ChemPhysMater 5 (2026) 472–484

Contents lists available at ScienceDirect

ChemPhysMater

journal homepage: https://www.keaipublishing.com/en/journals/chemphysmater/

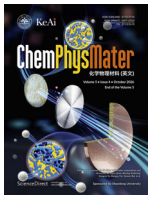

Research Article

Gigantochloa scortechinii-derived microcrystalline cellulose–Ag_2CO_3 composite photocatalyst for efficient paracetamol degradation under low-intensity of UVC irradiation

Nurul Syarima Nadia Sazman[a], Nor Husnina Nor Shamsi[a], Nur Hafiz Hussin[a], Mohamad Syafie Mahmood[a], Fariza Aina Abd Manan[a], Hamizah Mokhtar[b], Hartini Ahmad Rafaie[c], Shaari Daud[a], Zul Adlan Mohd Hir[a,*]

[a] Department of Chemistry, Faculty of Applied Sciences, Universiti Teknologi MARA Pahang, Bandar Tun Abdul Razak Jengka 26400, Malaysia
[b] Department of Civil Engineering, Faculty of Civil Engineering, Universiti Teknologi MARA Pahang, Bandar Tun Abdul Razak Jengka 26400, Malaysia
[c] Department of Physics, Centre of Foundation Studies, Universiti Teknologi MARA Selangor, Dengkil 43800, Malaysia

ARTICLE INFO

Keywords:
Density functional theory
Gigantochloa Scortechinii
Microcrystalline cellulose
Paracetamol
Silver carbonate

ABSTRACT

This study describes the facile fabrication of microcrystalline cellulose (MCC) from *Gigantochloa scortechinii* bamboo fibres serving as an electron mediator for Ag_2CO_3 photocatalyst. Comprehensive characterization techniques were used to illustrate the successful integration of Ag_2CO_3 onto MCC surfaces. The SEM images revealed homogeneous distribution of tiny rod-shaped Ag_2CO_3 nanoparticles on MCC's surfaces. Moreover, XRD verified phase-pure Ag_2CO_3 with crystallinity >70%, while the PL spectroscopy demonstrated suppressed emission intensity for MCC-Ag_2CO_3 and band gap narrowed from 2.8 to 2.6 eV. As shown by the band gap and PL analyses, the enhanced performance was ascribed to the remarkable rapid separation of electron and holes charge carriers, ease of electron migration, while highlighting the presence of MCC as electron mediators in the composite photocatalyst. The paracetamol (PCM) was used as targeted pollutant for the photocatalytic evaluations assisted by a relatively low UVC light intensity (9 W). With a rate constant of 9.4×10^{-3} min^{-1}, which was 1.5 times higher than that of pure Ag_2CO_3, the MCC-Ag_2CO_3 reached a notable 82% percentage of degradation under normal conditions. From DFT calculation, the MCC-Ag_2CO_3 shows orbital hybridization, reducing band gap and recombination while boosting charge separation via conductive channels and localized mid-gap states. The reactivity was dominated by photogenerated holes, followed by superoxide radical anions and hydroxyl radicals (h_{vb}^+ > $\bullet O_2^-$ > •OH) and the degradation was sustained with >50% efficiency over five consecutive cycles.

1. Introduction

The escalation of diverse anthropogenic activities has intensified water contamination into a central ecological crisis facing today's society [1]. The contamination of water sources by pharmaceutical residues have surfaced as a pressing ecological issue, fuelled by surging worldwide drug consumption and the inefficiency of conventional wastewater treatment processes in eradicating such pollutants. Within these emerging contaminants, paracetamol stands out as one of the most frequently detected analgesics in surface waters, effluents, and even drinking water supplies [2]. The occurrence of these pharmaceuticals in potable water poses significant risks to human health, including fostering antibiotic resistant bacteria, endocrine system disruption, aquatic toxicity, and potential genotoxic effects [3].

Advanced oxidation processes (AOPs) have gained prominence for eliminating recalcitrant organic pollutants owing to their ability to generate highly reactive species such as hydroxyl and superoxide radicals [4]. Heterogeneous photocatalysis, in particular, developed as an effective AOPs that leverages semiconductor oxides activated under light irradiation. These semiconductors have the potential to produce strong oxidizing species to mineralize organic contaminants like antibiotics into non-toxic end-products, which offers significant benefits for environmental remediation [4–6]. In brief, the semiconductors are activated by a light with corresponding energy exceeding the semiconductor's band gap, causing excitation of electrons from the valence band (vb) to the conduction band (cb), thus generating electron-holes (e_{cb}^-/h_{vb}^+) pairs on the photocatalyst's surface. The high oxidation potential of h_{vb}^+ would react with adsorbed water/OH^- to produce hydroxyl rad-

* Corresponding author.
E-mail address: zuladlan@uitm.edu.my (Z.A.M. Hir).

https://doi.org/10.1016/j.chphma.2026.03.011
Received 15 January 2026; Received in revised form 13 March 2026; Accepted 31 March 2026
Available online 16 April 2026
2772-5715/© 2026 The Authors. Publishing Services by Elsevier B.V. on behalf of KeAi Communications Co. Ltd. This is an open access article under the CC BY-NC-ND license (http://creativecommons.org/licenses/by-nc-nd/4.0/)

icals (•OH) which participates in the degradation process. While the e_{cb}^- would also react with adsorbed oxygen to produce superoxide radical anions ($\bullet O_2^-$) with sufficient reduction potential to degrade organic contaminants. The relevant basic reactions proceed as follows [7–9]:

$$h\upsilon + \text{semiconductor oxide} \rightarrow \text{semiconductor oxide } (e_{cb}^-/h_{vb}^+), \quad (1)$$

$$h_{vb}^+ + OH^- \rightarrow \bullet OH, \quad (2)$$

$$h_{vb}^+ + H_2O \rightarrow \bullet OH + H^+, \quad (3)$$

$$e_{cb}^- + O_2 \rightarrow \bullet O_2^-, \quad (4)$$

$$h_{vb}^+ + \text{organic contaminant} \rightarrow \text{intermediates} + CO_2 + H_2O, \quad (5)$$

$$\bullet OH + \text{organic contaminant} \rightarrow \text{intermediates} + CO_2 + H_2O, \quad (6)$$

$$\bullet O_2^- + \text{organic contaminant} \rightarrow \text{intermediates} + CO_2 + H_2O. \quad (7)$$

Among diverse photocatalysts, silver carbonate (Ag_2CO_3) has garnered considerable interest due to its strong oxidizing potential and sensitivity to visible light, attributed to its narrow band gap (~2.1 eV). Despite its merits, Ag_2CO_3 suffers from significant limitations such as low structural stability, rapid photo-corrosion making it photochemically unstable, alongside particle aggregation, which hamper its long-term effectiveness and reuse potential [10,11]. To address these limitations, the development of composite system wherein Ag_2CO_3 is deposited on a stable and reactive carrier material has proven effective. Microcrystalline cellulose (MCC), obtained through partial cellulose depolymerization, constitutes a sustainable, biodegradable, renewable, and crystalline biopolymer rich in surface hydroxyl moieties. These features allow MCC to serve as a supportive matrix that can disperse photocatalysts uniformly, inhibit agglomeration, improve photocatalyst's recyclability and facilitate interfacial charge transfer [8,12]. Additionally, MCC itself has shown potential in enhancing the uptake of contaminants, originated from the MCC porous structure providing additional active sites for photocatalysis [13]. Thus, these properties of MCC attributes to enhance the adsorption of pollutants and improve photocatalytic activity in composite materials. Moreover, employing lignocellulosic biomass, particularly bamboo, as a raw material for MCC production offers additional sustainability gains. Furthermore, *Gigantochloa scortechinii*, a fast-growing bamboo species native to Southeast Asia, is a underutilized source of high grade cellulose [14]. Ultimately, synthesising MCC from the bamboo, not only adds value to agricultural waste but also aligns with green chemistry principles in photocatalyst fabrication.

In recent years, several studies have reported composite of MCC and photocatalysts such as MCC/ZnO [8], MCC/Cu_2O/GO [13], $BiVO_4$@diatomite/MCC/PVBCFs [15], MCC/MT-MB aerogel [16] on the photocatalytic performance for degrading the organic pollutant. For example, MCC-based supports have been shown to significantly enhance charge separation and reaction kinetics when coupled with ZnO photocatalysts through hydrogen bonding networks, leading to improved degradation of organic pollutants [8,17]. Amaly et al. successfully synthesized an MCC/MT-MB aerogel that achieved 97% removal of tetracycline (TC) within 120 min under UVA irradiation combined with adsorption. This superior adsorption-degradation performance stems from the intimate contact between the photosensitizer methylene blue (MB) and TC, facilitated by multiple mechanisms including pore filling, electrostatic attraction, and specific metal complexation. As MCC aerogel serves as an ideal support for such photosensitizers and colloidal particles due to its cellulose structure, lightweight/high-strength properties, low cost, non-toxicity, and water processability, enabling enhanced photocatalytic pollutant remediation [16]. Furthermore, Previously, the fabrication of MCC/Cu_2O/GO composite foams demonstrated excellent photodegradation of methylene blue (MB) up to 78%. The enhanced performance is primarily attributed to the foam's porous structure and the synergistic interaction between MCC, Cu_2O, and GO, which functions as a 'micro-reactor' during MB degradation [13]. Unfortunately, while recent studies have demonstrated MCC's photocatalytic potential, they exhibit several limitations including required high-intensity UVA irradiation and organic photosensitizers, limiting practical deployment. Notably, only a few literature reports employ paracetamol (PCM) as the target pollutant.

Therefore, this study aims to synthesize and evaluate an innovative Ag_2CO_3-based photocatalyst dispersed on MCC derived from *Gigantochloa scortechinii* bamboo fibres for PCM photodegradation under low UVC light intensity (9 W). The research focuses on examines the morphological, compositions, structural, chemical state, recombination behaviours, functionalities, and optical characteristics of the composite photocatalyst while assessing its photocatalytic performance, photostability, and mechanism of degradation through radical scavenger analysis. By leveraging the synergistic effects between Ag_2CO_3 and bamboo-derived MCC, the study promotes a sustainable and efficient material for treating pharmaceutical wastewater via heterogeneous photocatalytic process.

2. Experimental

2.1. Materials

Microcrystalline cellulose was obtained from the extraction of raw bamboo fibre (*Gigantochloa scortechinii*) as previously reported by Sazman et al. [18]. Silver nitrate ($AgNO_3$, purity ≥99%) and sodium carbonate (Na_2CO_3, purity ≥99%) were supplied by R&M Chemicals (Malaysia). All reagents were purchased from R&M Chemicals, and they have been used just as they were supplied with no purification process. Paracetamol (PCM) was obtained from a local pharmacy in Malaysia. Throughout the research, deionized water was utilized.

2.2. Preparation of MCC-Ag_2CO_3 composite photocatalyst

The preparation of the MCC-supported Ag_2CO_3 photocatalyst was carried out via facile chemical precipitation technique. 0.1 g MCC was dispersed in 100 mL deionized water by ultrasonication (30 min), followed by sequential addition of 3.4 g $AgNO_3$ (0.02 mol, 0.2 M) and 1.06 g Na_2CO_3 (0.01 mol, 0.1 M) under vigorous magnetic stirring in complete darkness for 1 h at room temperature. The obtained precipitate was collected and washed with 100 mL deionized water thrice to remove any impurities. Following that, the product was dried in an oven at 55 °C overnight and the resultant sample was labelled as MCC-Ag_2CO_3. Similar experimental procedure was used without the addition of MCC for the preparation of pure Ag_2CO_3.

2.3. Photocatalyst characterizations

The surface morphological and elemental compositions were examined via scanning electron microscope with an energy dispersive X-ray analyzer (SEM-EDX, TESCAN VEGA3). The phase purity and crystalline characteristic of the prepared MCC-supported Ag_2CO_3 photocatalysts were characterized using X-ray diffraction (XRD) (PAN analytical with Cu-Kα radiation probe beam of 1.54056 Å wavelength) with 10°–70° range. The functional groups present in the composite photocatalyst were examined using Fourier transform infrared (FT-IR) equipped with the attenuated total reflection (ATR) accessory, between 4000 and 500 cm^{-1}. The Photoluminescence (PL) spectra measurement was performed on a fluorescence spectrophotometer (LS55, PerkinElmer, USA) at room temperature using an excitation source of He-Cd laser line 350 nm to examine the separation and recombination reactions of the charge carriers at the interface. The samples' chemical states were

probed using X-ray photoelectron spectroscopy (XPS) and the measurements were further conducted by an ARL Quant X-ray photoelectron spectrometer using Al Kα X-ray ($h\upsilon$ = 1486.6 eV). The optical features of the products were characterized by Ultraviolet-visible Near Infrared Spectroscopy (UV–vis NIR, Lambda 1050, PerkinElmer Corp., USA) within the wavelength span from 200 to 800 nm.

2.4. Computational calculation using DFT analysis

Density functional theory (DFT) calculations via first-principles methods were utilized to probe the structural, electronic, and optical characteristics of pure Ag_2CO_3, MCC, and the MCC-Ag_2CO_3 composite photocatalyst. All computations were performed using the Cambridge Sequential Total Energy Package (CASTEP) module [19]. For constructing the model, bulk Ag_2CO_3 was cleaved along the (110) surface to create a three-layer slab model. A vacuum spacing of 12 Å was added to inhibit interactions between periodic images [20]. Later, the MCC was placed onto the Ag_2CO_3 (110) surface to form the composite structure, followed by full geometry optimization. The electronic structure was calculated by utilizing the generalized gradient approximation (GGA) with the Perdew–Burke–Ernzerhof (PBE) functional, along with ultrasoft pseudopotentials [21]. The Kohn–Sham equations were solved using a plane-wave basis set under periodic boundary conditions, with Bloch's theorem. Geometry optimization was performed by the Broyden–Fletcher–Goldfarb–Shanno (BFGS) minimization algorithm, ideal for unconstrained nonlinear optimization in crystalline systems. Brillouin zone integrations were performed by utilizing a Monkhorst–Pack k-point grid of $4 \times 1 \times 1$, with a plane wave energy cutoff of 630 eV. The convergence thresholds were set as follows; total energy tolerance of 5×10^{-7} eV per atom, maximum of 1000 self-consistent field (SCF) cycles, and residual stress under 0.1 GPa [22]. These computational parameters ensured accurate calculation of the systems' electronic wavefunctions, charge densities, and optical characteristics.

2.5. Photocatalytic performance and kinetic evaluation

The evaluation of photocatalytic activity was carried out in a 250 mL beaker. Meanwhile, a 100 mL of 10 mg/L PCM solution was used as the working solution, with the 0.2 g of the MCC-Ag_2CO_3 composite photocatalyst was added. The first 30 min of the experiment was left in the dark, without the aid of irradiation with continuous stirring to accomplish the adsorption-desorption equilibrium. Later, the experiment was exposed under the low UVC irradiation intensity (9 W, 254 nm), with the aid of oxygen supply and continuously stirred for 180 min. Throughout the experiment, 5 mL samples were taken every 30 min. The PCM absorbance was determined using a UV–vis Spectrophotometer (PerkinElmer Lambda 35) at λ_{max}= 243 nm. The degradation percentage and amount of degraded were calculated using the Eqs. (8) and (9). The photodegradation of PCM was proceeded with pure Ag_2CO_3 as a control, under the same experimental conditions.

$$\text{Degradation percentage } (\%) = \frac{(C_0 - C_t)}{C_0} \times 100\%, \tag{8}$$

$$\text{Amount of degraded } \left(\frac{\text{mg}}{\text{g}}\right) = \frac{(C_0 - C_t)}{\text{Mass of photocatalyst (g)}} \times \text{Volume(L)}. \tag{9}$$

The PCM removal kinetics were determined by utilizing the Langmuir–Hinshelwood first-order kinetics model, the equations as presented in Eqs. (10) and (11) [23,24];

$$r = -\left(\frac{dC}{dt}\right) = k_{obs}C, \tag{10}$$

$$\ln\left(\frac{C_0}{C_t}\right) = k_{obs}t, \tag{11}$$

where C_0 represents the PCM's initial concentration and C_t denotes the residual concentration at 30 min time interval, r denotes the reaction rate, and k_{obs} is the apparent pseudo-first-order rate constant (min^{-1}).

3. Results and discussion

3.1. Surface morphological, composition, and structural analyses

Fig. 1 shows the SEM results, morphology figures of (a) pure MCC, (b) pure Ag_2CO_3, (c) MCC-Ag_2CO_3 at 2k magnification, and (d) MCC-Ag_2CO_3 at 5k magnification, respectively. As presents in Fig. 1(a), it can be spotted that the individual pure MCC's particle possessed a diminutive stick-like structure with a rough surface with the diameter ranging from 5.18 to 11.11 μm. Accordingly, the small structure of MCC might be due to acid hydrolysis treatment that caused the long structure of cellulose broke into shorter parts [9,10]. Meanwhile, the structure of pure Ag_2CO_3 as illustrated in Fig. 1(b), shows an irregular, tiny rod shape, which is accordant with earlier studies [25]. Ganie et al. also reported in their study, that the obtained structure of Ag_2CO_3 is observed to be polyhedral rod-like microstructures exposing different facets to the surface [26]. Furthermore, the structure of the MCC-supported Ag_2CO_3 composite photocatalyst (Fig. 1(c)) shows a similar structure of both rough surfaces MCC's diminutive stick-like and the pure Ag_2CO_3's irregular, tiny rod shape. While in Fig. 1(d), MCC-Ag_2CO_3 composite photocatalyst at 5k magnification shows that Ag_2CO_3 homogeneously distributed on the pure MCC surfaces. It's been suggested that the pure MCC play the crucial role in order to enable the Ag_2CO_3 particles to distribute evenly onto its surfaces, while inhibit the particles agglomerate and able to have more access with light sources.

Meanwhile, the MCC-Ag_2CO_3 composites photocatalyst was further characterized by element mapping and EDX images as depicted in Figs. 1(e)–(i). From the mapping, it can be observed the elements of silver (Ag), oxygen (O) and carbon (C) in the composite photocatalyst and been represented by blue, green and red colours, accordingly, corresponding to pure MCC and Ag_2CO_3. As displayed in the Fig. 1(e), those elements were covered the whole profile completely showing a good dispersity and it can be concluded that the elements been distributed homogeneously. In addition, Fig. 1(e). reveals that the identified gold (Au) peaks are from the SEM's sputter coating, and with no additional peaks identified, the results affirm the samples' purity. Moreover, the determined percentages of Ag, O, and C contents were 30.80%, 51.27%, and 17.93% accordingly.

The X-ray diffraction (XRD) analysis was employed to examine the crystallinity and phase structure of as-prepared samples and Fig. 2 shows the XRD patterns of (a) pure MCC, (b) pure Ag_2CO_3, and (c) MCC-Ag_2CO_3 composite photocatalyst. The detected (200) and (110) lattice planes were attributed to cellulose's characteristic diffraction peaks (2θ) at 15.74° and 22.37°, as observed from the XRD spectra of pure MCC (Fig. 2(a)) [8]. Furthermore, the pure Ag_2CO_3's XRD spectra as shown in Fig. 2(b), revealing the diffraction peaks detected at 2θ values of 18.71° (100), 20.61° (020), 29.15° (011), 32.66° (−101), 33.75° (−132), 37.12° (−121), 39.70° (031), and 51.62° (150) with its possible correspond planes, respectively. The results obtained are in good agreement with monoclinic phase of Ag_2CO_3 (JCPDS No. 26-0399) [25,27,28]. Concurrently, it can be concluded that the MCC-Ag_2CO_3 composite photocatalyst (Fig. 2(c)) retained in its initial state based on the sample's diffraction peaks that corresponding to both pure MCC and pure Ag_2CO_3. Additionally, all the samples' XRD spectra represent a phase of excellent purity, as no distinctive peaks of any contaminants were found, further proving the EDX analysis. Meanwhile, the pure Ag_2CO_3 and MCC-Ag_2CO_3 composite photocatalyst spectra illustrate thin peaks, implying that they are both possessed a high crystallinity [29].

3.2. Chemical state, recombination behaviour, band gap energy, and functional group analyses

The chemical states and surface element composition of the MCC-Ag_2CO_3 composites photocatalyst were further investigated utilizing X-ray photoelectron spectroscopy (XPS) as shown in Fig. 3. The result of full XPS element analysis disclosed the existence of Ag 3d, O 1s, and

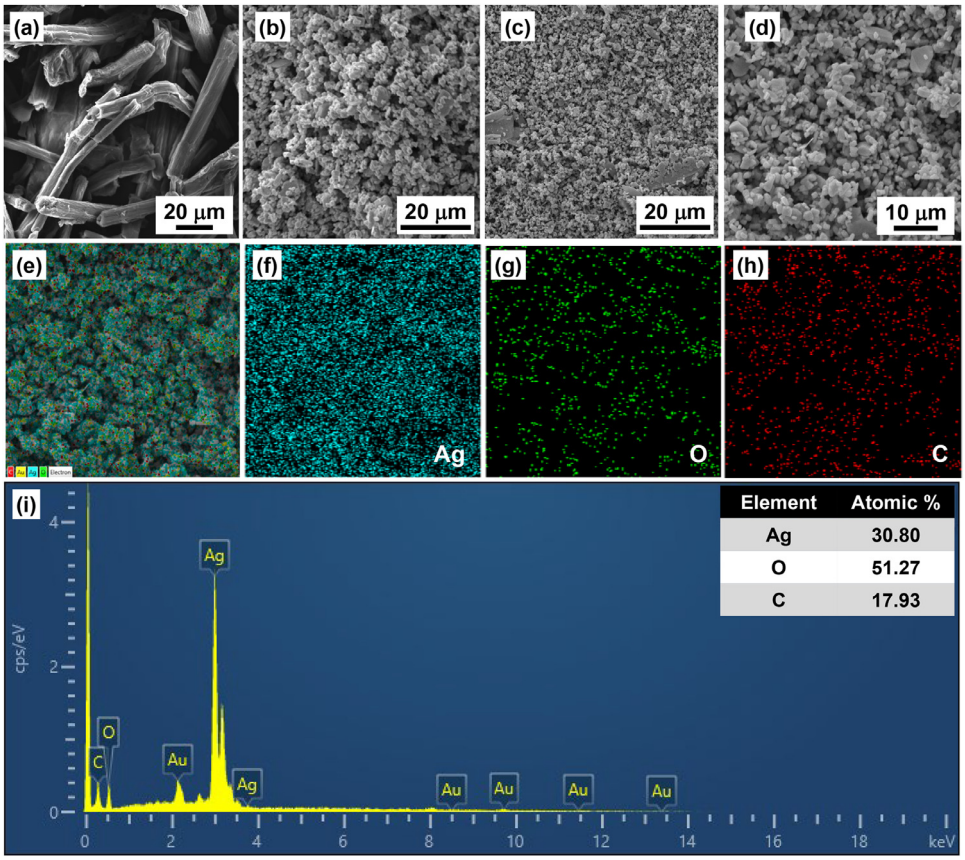

Fig. 1. SEM images of (a) pure MCC, (b) pure Ag_2CO_3, (c) MCC-Ag_2CO_3 composite photocatalyst at 2k magnification, and (d) MCC-Ag_2CO_3 at 5k magnification, (e) EDX analysis of selected image of the MCC-Ag_2CO_3 composite photocatalyst with corresponding elemental mapping images for (f) Ag, (g) O, (h) C, and (i) the elemental spectra and sample's composition.

C 1s elements based on those three detected distinct peaks with no other impurities found in the survey spectrum (Fig. 3(a)), which implies both pure MCC and pure Ag_2CO_3 are present in the composite sample. From the high-resolution XPS spectrum of C 1s spectrum alone in Fig. 3(b), three significant binding energies were identified at 284.8, 286.9 and 289.0 eV indicates the occurrence of C–C, C=O and O–C=O linkage [26,30]. In addition, Zhou and colleagues also mention in their study, that the peak at 284.8 eV can be associated to the species of amorphous, while the peak at 289.0 eV might be related to the Ag_2CO_3 peak for C [25]. The peaks with binding energies of 284.32 and 287.61 eV represent C–O and C–O bonding in Ag_2CO_3, respectively. energy peaks at 289.4, 286.2, and 284.6 eV confirm the presence of C–H, C–O, and C–C bonding of cellulose, respectively [31]. In Fig. 3(c), the deconvoluted spectra of O 1s reveal two peaks at 531.2 eV and a minor peak at 533.2 eV, confirming the occurrence of lattice oxygen in both pure MCC and Ag_2CO_3, oxygen physisorption, and O^{2-} in the hybrid linkage structure pertaining to the C–O in Ag_2CO_3 [25,26,32]. The high-resolution XPS spectrum of Ag 3d region as shown in Fig. 3(d) illustrates two main peaks located at 368.4 and 374.4 eV appointed to the Ag $3d_{5/2}$ and Ag $3d_{3/2}$ photoelectrons [32,33]. Meanwhile, previous studies also suggested that the Ag element appears as Ag^+ in the composite samples aligned with the peaks detected from the spectra [25,33,34]. In addition, the gap between the peaks of Ag 3d giving the standard difference value of Ag_2CO_3's binding energy which is 6.0 eV. This finding correlated with previous research done by Ganie and fellow worker [26].

The recombination behaviour of pure Ag_2CO_3 and MCC-Ag_2CO_3 composite photocatalyst was assessed using photoluminescence (PL) emission spectroscopy as presented in Fig. 4(a). This approach was used to analyse the separation and photoinduced charge carriers' transfer rate, specifically focusing on the photogenerated electron-hole (e_{cb}^-/h_{vb}^+) pairs migration and recombination rates [31]. Accordingly, the PL spectra are the resultant from the recombination of electron-hole pairs as the excited electrons return to its ground state. The PL intensity is inversely related to photocatalytic activity, as higher intensity reflects the higher recombination efficiency, leading to lower photocatalytic activity. Therefore, in this case, the PL peaks intensity serves as a reliable indicator of charge recombination dynamics [26]. As a high intensity peak observed from the pure Ag_2CO_3's PL spectra, it's been expected to have a low rate of electron-hole pairs migration and recombination rates. High PL peak intensities demonstrates photogenerated carriers readily recombine, and emitting bright fluorescence [27]. Moreover, Wang and colleagues reported that Ag_2CO_3 is an efficient catalyst, however its performance is hindered by the high rate of photoinduced charge carriers recombination [35]. In contrast, the MCC-Ag_2CO_3 composite photocatalyst exhibits low PL peak intensity, in brief the inclusion of MCC led to substantially reduce emission peaks than pure Ag_2CO_3. When the composite photocatalyst exposed to photon, the gradual recombination of charges caused the intensity to decrease [32]. And, the likelihood of photogenerated charge carrier separation is generally higher when PL intensity is lower [35]. This situation suggests a lower recombination rate of electron-hole pairs, can enhance the photocatalytic activity [8]. Meanwhile, high efficiency of charge separation consequently, high photocatalytic performance which can be attributed to reduced electron-hole (e_{cb}^-/h_{vb}^+) pairs recombination and enhanced charge separation at the interfaces [26].

The UV–vis spectroscopy was used in order to observe the optical properties of the pure Ag_2CO_3 and MCC-Ag_2CO_3 composite photocatalyst by examining their response to electromagnetic radiation, specifically visible and ultraviolet (UV) light. The Kubelka-Munk method was used to estimate the band gap energy of the pure Ag_2CO_3 and MCC-

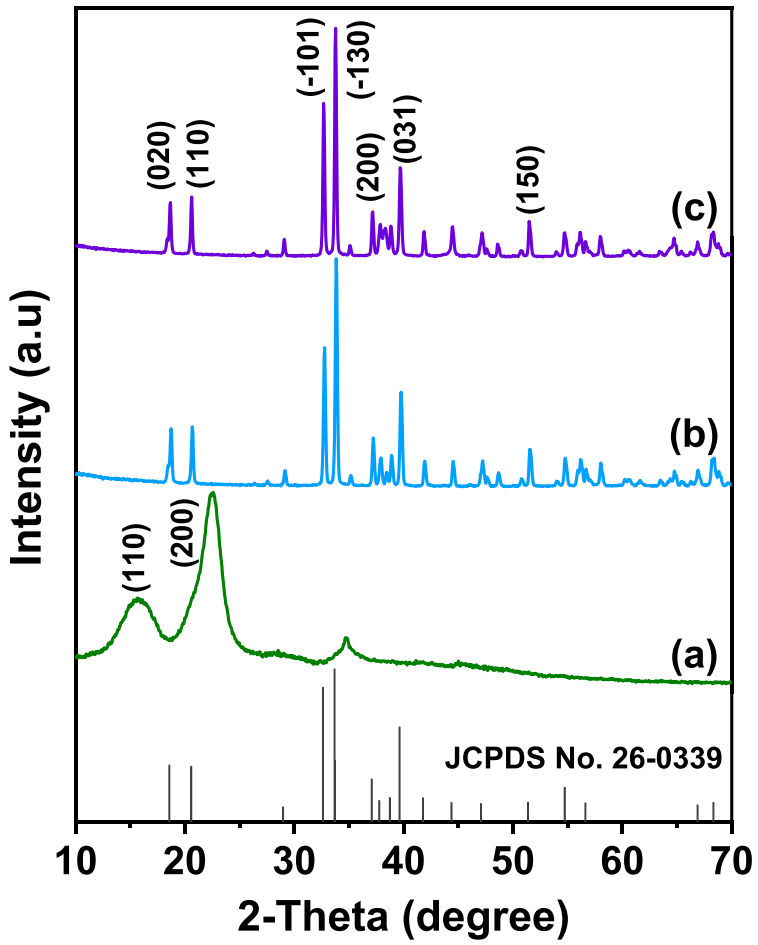

Fig. 2. XRD spectra of (a) pure MCC, (b) pure Ag_2CO_3, and (c) MCC-Ag_2CO_3 composite photocatalyst.

Ag_2CO_3 composite photocatalyst, with the corresponding equation as shown in Eq. (12) [26].

$$F(R)\cdot\ h\upsilon = \left(Ah\upsilon - E_g\right)^{\frac{n}{2}}, \tag{12}$$

where ν represents the light frequency, E_g is the energy difference between the conduction and valence bands h and A are the constants, $F(R)$ is the Kubelka-Munk function, and n indicates the nature of the electronic transition. The band gap (E_g) was determined from Tauc's plots by assuming ($n = 1$) for direct transitions, where it can be 1 for direct or 2 for indirect transitions depending on the sample's characteristics. Meanwhile, the plot of $[F(R)\cdot h\nu]^2$ (the Kubelka-Munk function multiplied by the photon energy) on the y-axis, against the photon energy ($h\nu$) on the x-axis were illustrated in Fig. 4(b). The band gap is determined by the extrapolation of the linear region of the plot to the x-axis [26,29]. The estimated band gap values of pure Ag_2CO_3 and MCC-Ag_2CO_3 composite photocatalyst were 2.8 and 2.6 eV, respectively. The decrease in the band gap is attributed to the introduction of MCC into the matrix of pure Ag_2CO_3. The results indicate that MCC-supported Ag_2CO_3 exhibits stronger visible light responsiveness and higher photocatalytic activity compared to pure Ag_2CO_3. Furthermore, higher photocatalytic performance can be achieved through reduced interfacial barriers and excellent electronic coupling, which later will enhance the production of photogenerated electron-hole (e_{cb}^-/h_{vb}^+) pairs [34]. Ganie and coworkers also suggest that scattered light travels along a longer optical path, enhancing absorption, while materials having resilient photon absorption in the visible band are more beneficial for solar energy applications, promoting photostability and photocatalytic performance [26].

Fig. 5 shows illustrative FTIR emission spectrum of (a) pure MCC, (b) pure Ag_2CO_3, and (c) MCC-Ag_2CO_3 composite photocatalyst. These spectra were analysed to study the chemical bond vibration modes in the synthesized samples. From Fig. 5(a), pure MCC presents the peaks of FTIR spectrum at 3300, 2895, 1428, 1316, 1030 and 897 cm^{-1}. Accordingly, strong band in the 3400–3300 cm^{-1} region corresponding to the hydroxyl groups (–OH) stretching in cellulose [36]. Moreover, the detected bands around 1360 cm^{-1}, are associated with the bending vibrations of the C–H bond in the cellulose and hemicellulose structure (polysaccharide aromatic ring) [14]. Furthermore, the band at 1631 cm^{-1} is attributed to the C=O stretching vibration of the carboxylate group, while the broad peak between 1030 and 1051 cm^{-1} corresponds to the C–O stretching vibration [37]. It was reported that the absorption band at 897 cm^{-1} corresponds to the typical cellulose structure, associated with the β-glycosidic linkages of cellulose, involving anomeric C1-H bending and C1–O–C4 glycosidic deformation [8,38]. Additionally, pure Ag_2CO_3 (Fig. 5(b)) exhibits the distinctive peaks at ~711, ~801, ~1071, and ~1315 cm^{-1} which can be observed from the typical spectrum of Ag_2CO_3, attributed to the vibrational modes of carbonate ion (CO_3^{2-}) group in Ag_2CO_3 [26,34]. The peaks observed between 1350–1500 cm^{-1} and around 800 cm^{-1}, attributed to the asymmetric stretching and symmetric deformation vibrations of the CO_3^{2-} [33]. Meanwhile, in Fig. 5(c) the spectra of MCC-Ag_2CO_3 composite photocatalyst presents peaks that parallel with pure Ag_2CO_3, except having a slightly increased in wavenumber as only small amount of MCC added into the composite samples. The existence of CO_3^{2-} in the composites is proved from the peaks at 1317 and 1071 cm^{-1} [28]. Accordingly, the characteristic peaks of CO_3^{2-} at 1317, 1071, 801, and 721

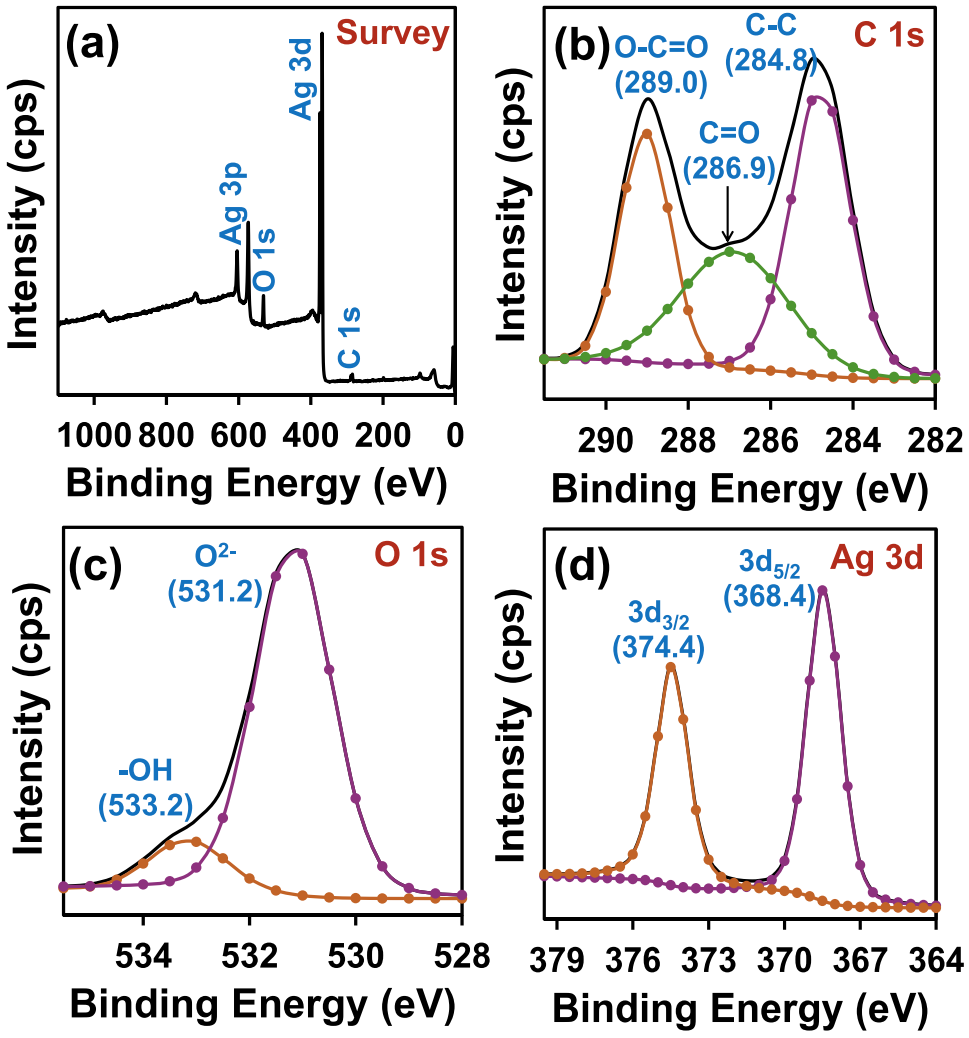

Fig. 3. X-ray photoelectron spectra of (a) survey spectrum, (b) C 1s, (c) O 1s, and (d) Ag 3d spectrums of MCC-Ag_2CO_3 composite photocatalyst.

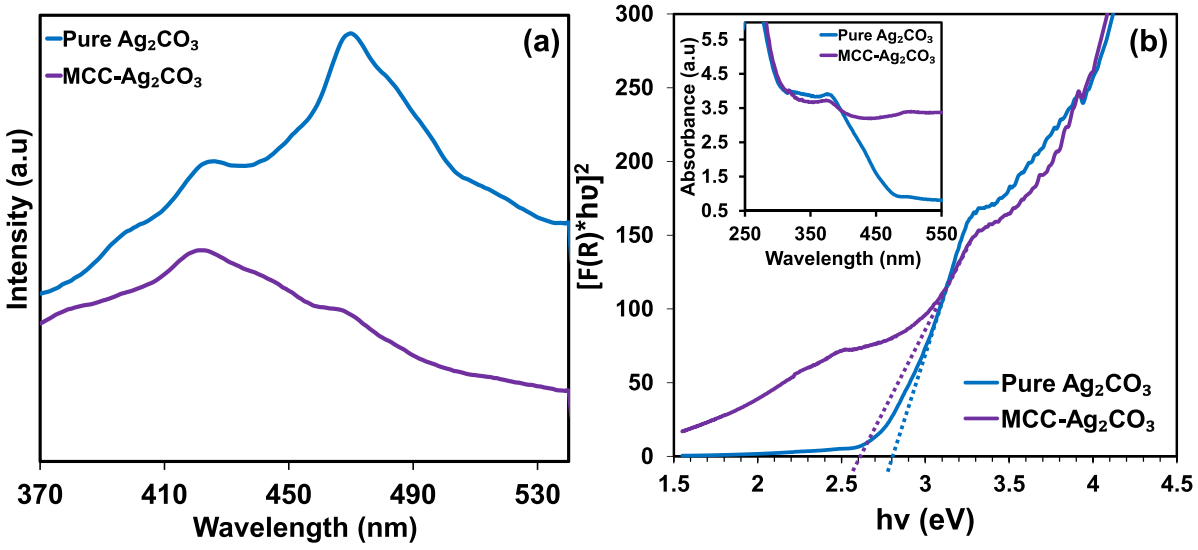

Fig. 4. (a) PL spectra, and (b) band gap energy of pure Ag_2CO_3 and MCC-Ag_2CO_3 composite photocatalyst.

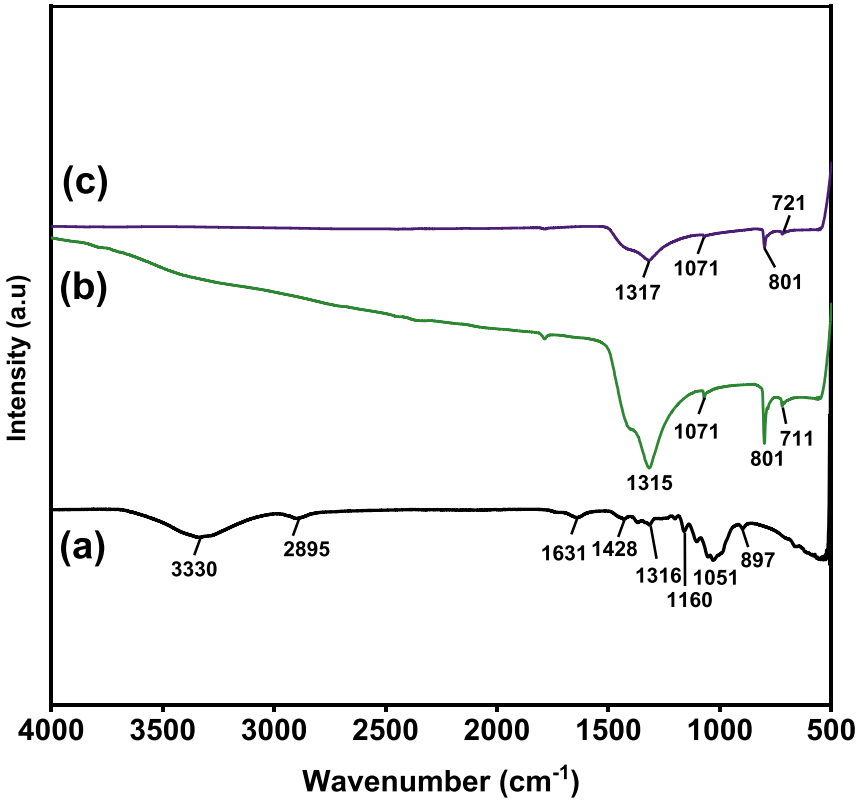

Fig. 5. FTIR spectra of (a) MCC, (b) pure Ag_2CO_3, and (c) MCC-Ag_2CO_3.

cm^{-1} are also visible [9]. Additionally, the slight peak shifted at 1317 cm^{-1} remain detectable, proving the interaction of Ag_2CO_3 and MCC. As previous study have reported, the characteristic Ag_2CO_3 absorption peak at 1373 cm^{-1} becomes blunt, weakened in intensity, and slightly shifted, providing evidence of chemical interactions between Ag_2CO_3 and the $ZnFe_2O_4$/bentonite components [5]. In summary, the FTIR spectra of the MCC-Ag_2CO_3 composite photocatalyst closely resemble those of pure Ag_2CO_3, suggesting that the incorporation of MCC does not significantly alter the peaks of Ag_2CO_3 in the composites.

3.3. Density functional theory (DFT) analysis

The calculated band structure of Ag_2CO_3 shows a narrow indirect band gap of around 0.460 eV, with the valence band mainly derived from Ag 4d and O 2p states, while the conduction band edge consists largely of C 2p states. This narrow gap suggests that Ag_2CO_3 can readily generate electron-hole pairs under visible-light irradiation, which is advantageous for photocatalysis as shown in Fig. 6 [39]. However, the high density of states around the Fermi level also implies a high probability of rapid electron-hole recombination. Such recombination reduces the availability of long-lived charge carriers required for redox reactions, which can limit the standalone photocatalytic efficiency of Ag_2CO_3 despite its favourable light absorption.

From Figs. 6(a)(b), it could be concluded that MCC optically inactive under visible light as it possessed a wide band gap of ~4.194 eV. The valence band primarily consists of O 2p states augmented by contributions from H 1s orbitals, whereas the conduction band arises from C 2p states. This pronounced band gap characteristic leads to insulating properties, thereby yielding minimal inherent photocatalytic performance. Despite this limitation, MCC demonstrates excellent chemical stability, environmental benignity, high porosity surfaces and functionalization, positioning it as an ideal support material. The primary role of MCC is indeed not to facilitate direct charge generation but rather to serve as a supportive matrix that accommodates active photocatalysts, improves dispersibility, mitigates agglomeration, and supplies reactive sites for nanoparticle anchoring [40].

As depicted in Figs. 6(c)–(f), the formation of MCC-Ag_2CO_3 composite fundamentally modifies the electronic structure, narrowing the band gap from 0.460 to 0.028 eV. This exceptional narrow band gap arises from strong interfacial hybridization between Ag 4d, O 2p, and C 2p states, as demonstrated in the density of states (DOS) profiles where these orbitals make substantial contributions near the Fermi level [20,41]. Such hybridization enables efficient charge dispersion at the interface, improving electrical conductivity and facilitating charge transfer [42]. In a photocatalytic context, this configuration broadens light absorption into the visible spectrum, meanwhile the intimate MCC-Ag_2CO_3 contact helps suppress the electron recombination by enabling spatial separation of photogenerated carriers. Not only the MCC matrix can stabilize Ag_2CO_3 but it also can create an interfacial defect state that trap charges, extending carrier lifetimes. Consequently, the MCC-Ag_2CO_3 composite photocatalyst is expected to outperform both pristine Ag_2CO_3 and MCC in photocatalytic performance, as it combines efficient visible-light absorption, improved charge transport, and enhanced stability.

A noticeable difference was observed between the experimental optical band gaps (2.8 eV for Ag_2CO_3 and 2.6 eV for MCC–Ag_2CO_3) and the DFT-calculated electronic band gap (~0.460 eV for Ag_2CO_3). This difference is expected, as standard GGA–PBE calculations are known to underestimate band gaps due to limitations in describing exchange–correlation effect. This can be seen from research done by Hassan et al. [39]. Moreover, the calculated value represents the electronic band gap of an ideal structure, whereas the experimental band gap obtained from Tauc plots (Fig. 4(b)) reflects the optical response of real materials, which includes effects such as defects, lattice interactions and excitonic transitions. Structural defects and surface imperfections can introduce localized energy states that influence optical absorption behaviour, while lattice interactions such as phonon coupling may shift transition energies into real materials. In addition, excitonic effects, arising from

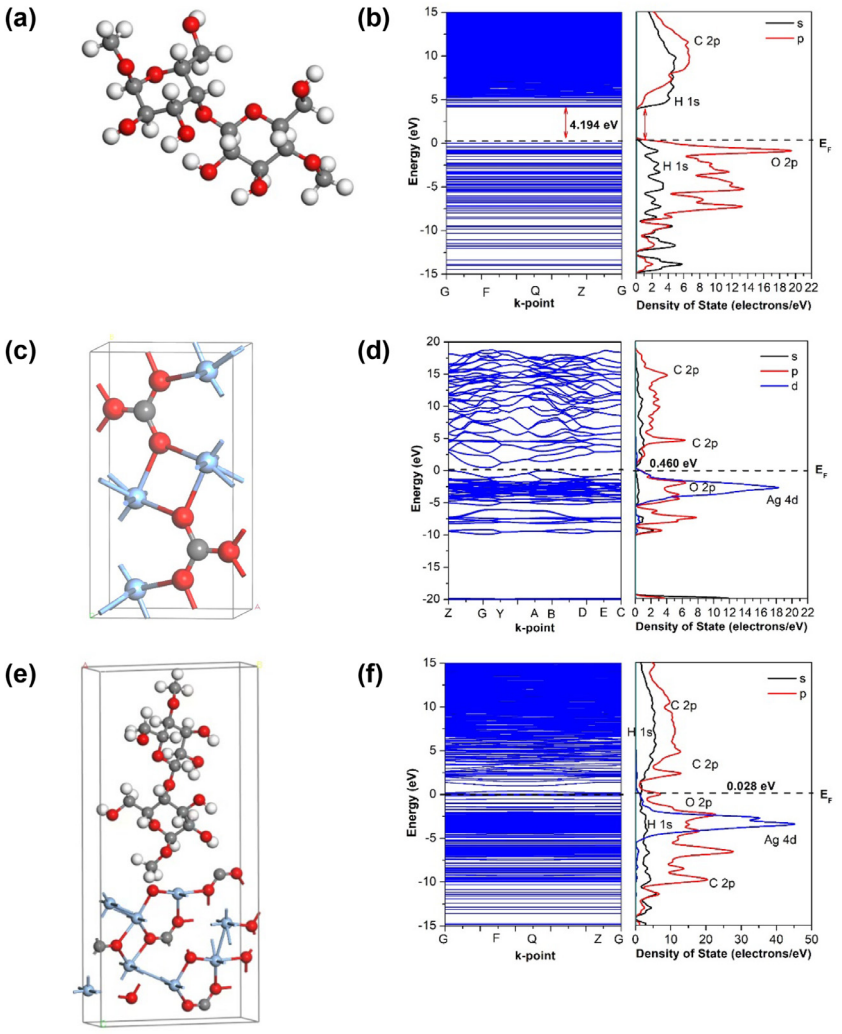

Fig. 6. The crystal structures, calculated electronic band structures, and density of states of (a)(b) MCC, (c)(d) pure Ag_2CO_3, and (e)(f) MCC-Ag_2CO_3 composite photocatalyst.

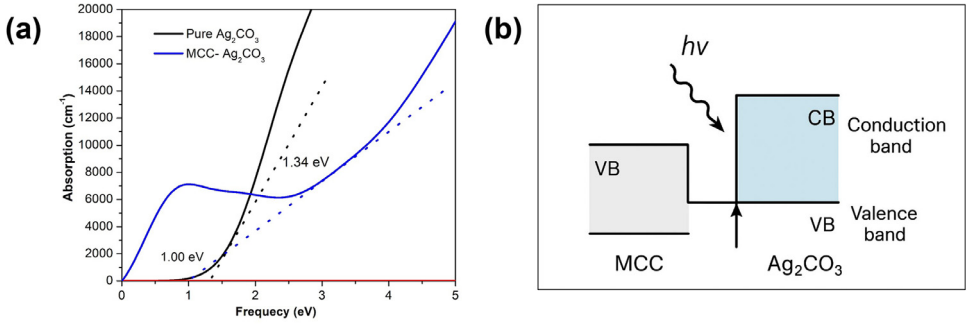

Fig. 7. (a) The optical band gap of Ag_2CO_3 and MCC-Ag_2CO_3 composite photocatalyst, and (b) schematic energy band diagram of MCC incorporation modifies the photocatalytic behaviour of Ag_2CO_3.

electron-hole interactions after photoexcitation can further modify the optical response by increasing the apparent transition energy. These real-material effects are typically not captured in first-principle DFT calculations, leading to wider experimentally observed optical band gaps [39,41]. It is also imperative to highlight that band gap obtained in DFT calculation is an indirect band gap, which may produce distinct outcome as compared to experimental observations.

It can be observed in Fig. 7, the absorption spectra of pure Ag_2CO_3 and MCC-Ag_2CO_3 composite photocatalyst clearly demonstrate the influence of MCC on the optical properties. Pure Ag_2CO_3 (black line) shows a sharp absorption edge corresponds to optical band gap approximately ~1.34 eV, implying its ability to absorb visible light at 925 nm. However, as Ag_2CO_3 is combined with MCC (blue line), the absorption edge is shifted towards a lower energy approximately ~1.00 eV, indicating a red-shift and narrowing of the band gap (Fig. 7(a)). This shift suggests that the MCC may introduce additional electronic interactions between Ag_2CO_3, through interfacial charge transfer and orbital hybridization, allowing the composite to use a broader portion of the

solar spectrum, including near-infrared light. These findings align with results reported by Qiu et al., who demonstrated a successful develops of a built-in electric field at the interface, oriented from g-C_3N_4 to Ag_2CO_3 [9]. Furthermore, the MCC-Ag_2CO_3 composite shows higher absorption intensity over the entire measured energy range, implying on a stronger photon-harvesting capability. These findings are consistent with the earlier band structure and DOS results, where the incorporation of MCC was shown to reduce the band gap and create mid-gap states that enhance light absorption. Thus, the absorption analysis proves that the MCC significantly enhances the light-harvesting efficiency of Ag_2CO_3, making the composite photocatalyst more ideal for the photocatalytic degradation applications.

This schematic energy band diagram shows a clear visualization of how the incorporation of MCC can modifies the photocatalytic behaviour of Ag_2CO_3 (Fig. 7(b)). The conduction band (CB) and valence band (VB) positions determine the pure Ag_2CO_3 intrinsic band gap (~1.34 eV), which only allow limited absorption of visible light [39]. As combined pure Ag_2CO_3 with MCC, interfacial charge transfer occurs at the MCC-Ag_2CO_3 composite interface due to orbital hybridization and surface electronic coupling. This interaction effectively narrows the band gap to ~1.0 eV, as proved by absorption spectra, enabling the composite to absorb a broader range of photons, including low-energy visible to near-infrared light [9]. Furthermore, the band alignment suggests that the MCC facilitates electron transfer by acting as a conductive support while reduces recombination of electron–hole, thus enhancing the overall photocatalytic degradation efficiency. The correlation between this band diagram with the absorption results, it can be observed that the MCC-Ag_2CO_3 composite possesses superior light-harvesting capability and superior charge carriers' separation, which explains its great performance in photocatalytic degradation applications compared to pure Ag_2CO_3.

The lower transition energies observed in the DFT absorption spectra (~1.34 eV for Ag_2CO_3 and ~1.00 eV for MCC-Ag_2CO_3) can be attributed to the formation of interfacial electronic states after MCC incorporation. The interaction between Ag 4d, O 2p and C 2p (Fig. 6) introduces localized mid-gap states that allow additional low-energy electronic transitions. These transitions enhance light absorption in simulations but do not directly correspond to the intrinsic optical band gap measured experimentally. Comparable behaviour has been reported in Ag_2CO_3-based composites where interfacial coupling creates sub-band gap transitions without significantly altering the fundamental band structure. For instance, Qiu et al. [9] observed that although interface engineering enhanced light absorption through additional electronic states, the experimentally measured optical band gap remained within the typical semiconductor range of ~2.5–2.8 eV. Similarly, Sudhaik et al. [40] reported that cellulose-supported photocatalysts may exhibit improved electronic interactions and charge transfer pathways while maintaining relatively wide optical band gaps. These findings support the present observation that the reduced transition energies predicted by DFT are associated with interfacial electronic effects rather than a true narrowing of the fundamental band gap [9,40]. Therefore, the DFT results should be interpreted as evidence of enhanced interfacial charge transfer and electronic interaction within the MCC-Ag_2CO_3 composite, rather than as a direct prediction of its experimental optical band gap.

3.4. Photocatalytic evaluation

The photocatalytic performance of the synthesized photocatalysts on PCM in aqueous solution was tested for 180 min with the aid of UVC light irradiation (Fig. 8). In photolysis process, PCM was found to be undegradable without the aid of the photocatalysts, showing that the PCM's molecules are rather stable and hard to degrade under environmental conditions [24]. The performance of PCM removal in aqueous solution was further tested with the pure Ag_2CO_3, and MCC-Ag_2CO_3 composite photocatalyst. Fig. 8(a) shows that MCC-Ag_2CO_3 composite photocatalyst had the lowest PCM concentration left (1.90 mg/L) instead of pure Ag_2CO_3 that still got rather high concentration of PCM (3.64 mg/L). These revealed that the photodegradation performance of PCM utilizing MCC-Ag_2CO_3 composite photocatalyst is 1.5 times higher than that of pure Ag_2CO_3 within 180 min of irradiation. The phenomenon could be due to the incorporation between MCC and Ag_2CO_3 which enhanced the PCM removal efficiency to the maximum of ~82%. While Fig. 8(b) indicates how much PCM was degraded for photolysis, pure Ag_2CO_3, and MCC-Ag_2CO_3 composite photocatalyst. A similar pattern can also be observed in the calculated data with MCC-Ag_2CO_3 yield the higher amount of PCM molecules degraded (10.8 mg/g) as compared to pure Ag_2CO_3 (8.6 mg/g).

Fig. 8(c) illustrates the linear graph of $\ln(C_0/C_t)$ versus degradation time, while it reveals the obtained results for PCM removal using both of pure Ag_2CO_3 and MCC-Ag_2CO_3 composite photocatalyst adhere to the Langmuir–Hinshelwood kinetic model [8]. The kinetic analysis indicates that the MCC-Ag_2CO_3 composite photocatalyst outperforms pure Ag_2CO_3 with a constant rate, k up to 9.4×10^{-3} min^{-1} highlighting that MCC-Ag_2CO_3 provides a rapid and more efficient photodegradation process (Fig. 8(d)). In this study, the enhanced of PCM's photodegradation efficiency might be due to the increased surface area of the samples. From SEM results, the Ag_2CO_3 particles distributed homogenously on the MCC surfaces. Consequently, the penetration of lights on the photocatalyst' surface also increased, thus escalated the production of reactive radicals' species and boosted the photodegradation efficiency. These findings are aligned with previously reported study, whereby the notable photocatalytic activity of TiO_2/cellulose is due to the aid of cellulose's superfine network structure, which allows TiO_2 nanoparticles to disperse across its surface resulting in maximized light irradiation [43]. Accordingly, the cellulose fibre proved to be an ideal substrate for nanometre-sized photocatalysts dispersion [44]. Moreover, the lower recombination rate of photogenerated electron-hole (e_{cb}^-/h_{vb}^+) pairs in the MCC-Ag_2CO_3 composite photocatalyst, as indicated by the PL analysis, may be one of the reasons for its highest photodegradation efficiency achieved. It was previously reported that when semiconductor particles are integrated to a support, e_{cb}^-/h_{vb}^+ may relocate to the support's surface, lowering the recombination rate and thereby promotes photocatalytic efficiency [45]. Furthermore, the smaller value of band gap calculated for the MCC-Ag_2CO_3 composite photocatalyst (2.6 eV) was proven enhancing the photocatalytic efficiency. This is due to its capability to absorb more lights thus increase the production of photogenerated electrons and holes pairs.

3.5. Photocatalytic mechanism

The radical scavenging experiment was carried out to identifies the active species accountable for the PCM's photodegradation performance by the MCC-Ag_2CO_3 composite photocatalyst, while elucidating the plausible mechanism of the complex e_{cb}^-/h_{vb}^+ transfer process (Fig. 9) [29]. In this experiment, 10 mL each of tert-butanol (TB), benzoquinone (p-BQ), and ethylenediaminetetraacetic acid (EDTA) were added to PCM working solution as hydroxyl (•OH), superoxide ($\bullet O_2^-$), and hole (h_{vb}^+) radical scavengers, accordingly [23], meanwhile the system was exposed for 180 min under UVC irradiation. Fig. 9(a) shows the effects of different trapping agents on the photodegradation of PCM in an aqueous solution. It was observed that with the addition of EDTA, p-BQ, and TBA, the photodegradation percentage of PCM were reduced to 67.0%, 57.16%, and 38.6%, accordingly. From the results, as compared to scavenger-free MCC-Ag_2CO_3 composite photocatalyst, the degradation of PCM is retarded in the presence of all the three scavengers indicating that all of them are active species. However, it is seen that degradation is more quenched by EDTA and PB suggesting that h_{vb}^+ and $\bullet O_2^-$ radicals species play more significant role [29]. Moroever, the –OH groups on MCC-Ag_2CO_3 composite photocatalyst' surfaces react with photogenerated holes (h_{vb}^+) to produce hydroxyl radicals (•OH), which can effectively break down PCM molecules (Fig. 9(b)). This interaction enhances the photocatalytic activity of MCC-Ag_2CO_3 composite

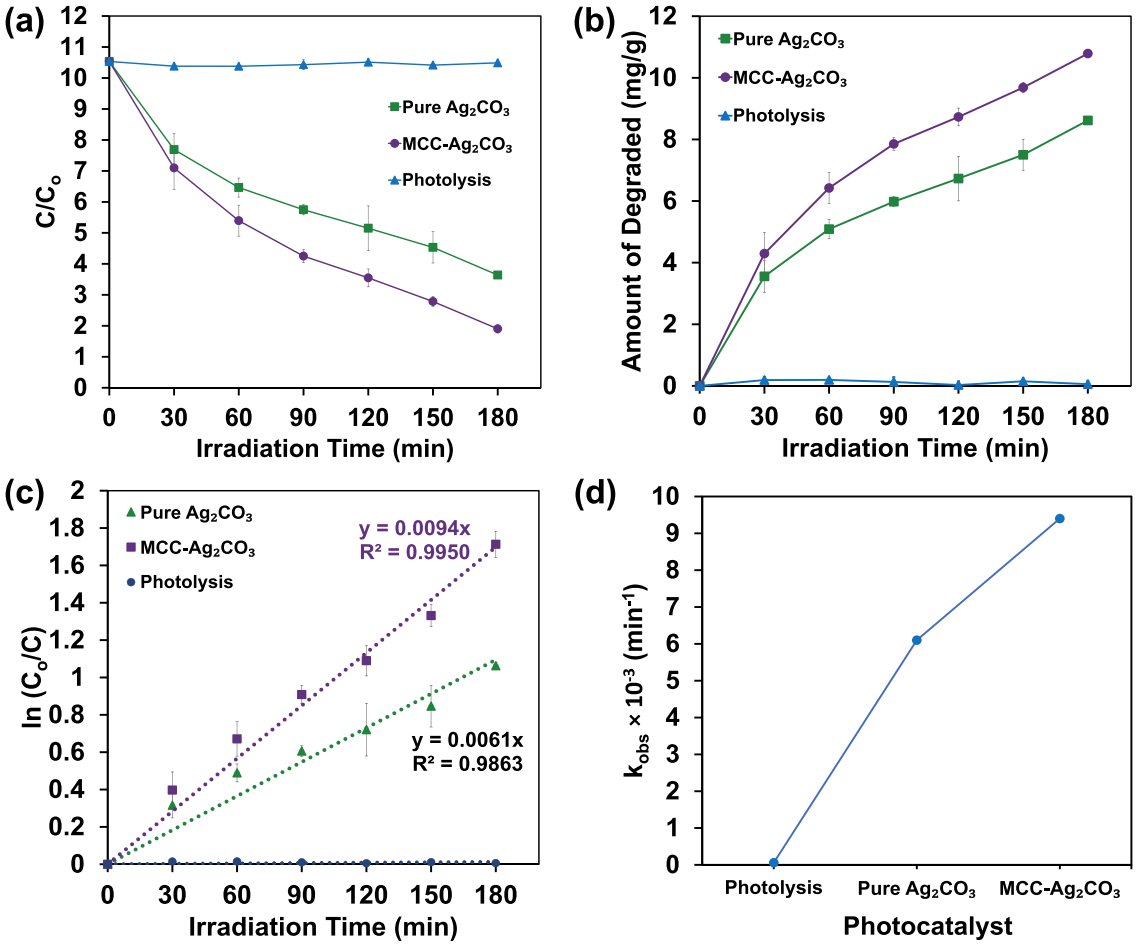

Fig. 8. (a) Degradation efficiency, (b) amount of degraded, (c) kinetic of the disappearance of PCM, and (d) pseudo first-order rate constant by photolysis, pure Ag_2CO_3, and MCC-Ag_2CO_3 composite photocatalyst. [PCM] = 10 mg/L, pH = 6.8, mass = 0.2 g.

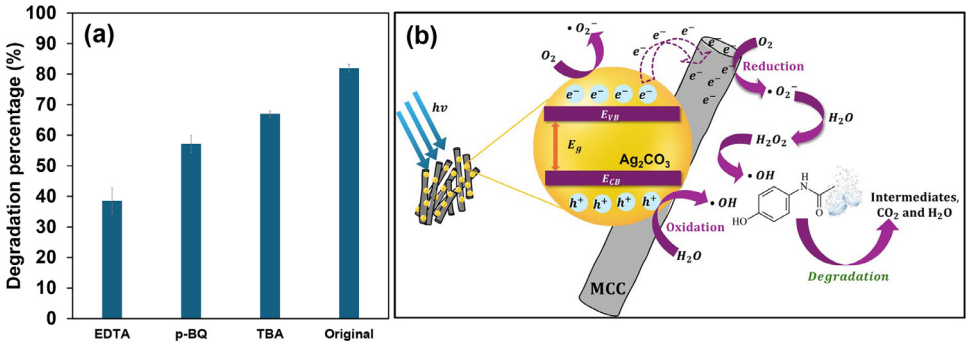

Fig. 9. (a) Degradation percentage of PCM by MCC-Ag_2CO_3 composite photocatalyst in the presence of different scavengers under UVC irradiation, and (b) plausible mechanism for the degradation of PCM. [PCM] = 10 mg/L, pH = 6.8, mass = 0.2 g.

photocatalyst, aiding in the degradation of organic pollutants [46]. It is essential to highlight that, although various reactants within the system may facilitate the breakdown of PCM indirectly by producing hydroxyl radicals (•OH), these radicals remain the primary active species responsible for the direct decomposition of PCM [47].

From the above experimental analyses discussed above, a plausible photocatalytic reduction mechanism of PCM in aqueous phase by the MCC-Ag_2CO_3 composite photocatalyst follows the mechanism outlined below. In brief, when a photocatalyst is exposed to light with energy matches or surpasses the photocatalyst's band gap, the electrons are excited from the valence band (vb) to the conduction band (cb), resulting in the formation of electron-hole pairs (e_{cb}^- and h_{vb}^+) on the Ag_2CO_3 surface as depicted in (Eq. (13)) [8,9]. Moroever, as the Ag_2CO_3's valence band maximum lies at a more positive potential than both the H_2O/O_2 and OH^-/H_2O redox levels, enabling photo-generated h_{vb}^+ to directly oxidize H_2O into •OH radicals [48,49]. The h_{vb}^+ exhibit strong oxidizing power, allowing them to serve as oxidants and rapidly react with H_2O, to produce •OH, hydrogen ions (H^+) or directly oxidize the targeted organic pollutants (Eqs. (14), (18), (19)) [50]. Meanwhile, the e_{cb}^- serve as reducing agent owing to their high reduction potential, reacting with dissolved O_2 in water or surface-adsorbed O_2 on the photocatalyst's surface to yield superoxide radicals anions ($•O_2^-$) or hydroperoxide radicals (HO_2^-) (Eqs. (15)–(17)) [8,48]. Accordingly, only Ag_2CO_3's h_{vb}^+ can oxidize OH^- and H_2O to generate •OH rad-

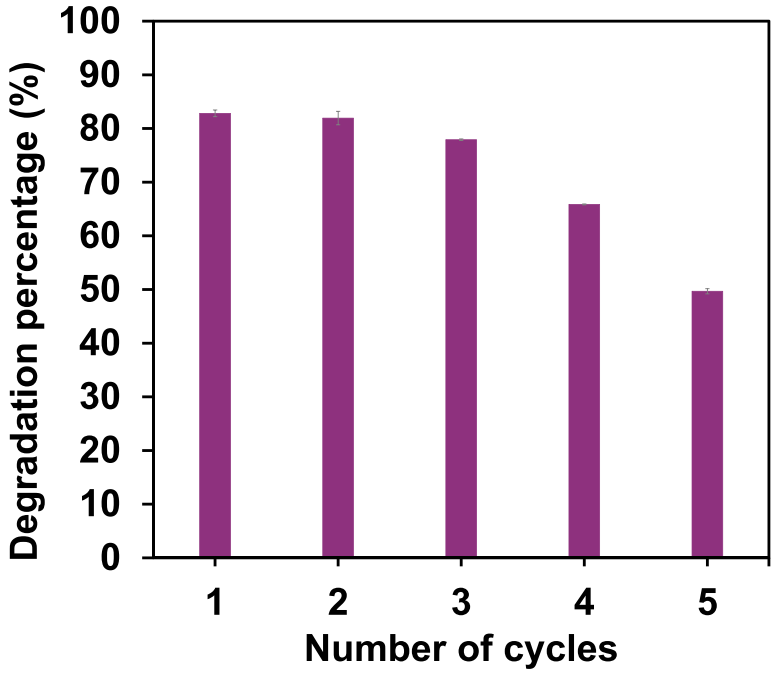

Fig. 10. Photostability of MCC-Ag_2CO_3 composite photocatalyst under UVC irradiation. [PCM] = 10 mg/L, pH = 6.8, mass = 0.2 g.

icals, while e_{cb}^- trapped by MCC, facilitates the conversion of O_2 to $\bullet O_2^-$ [48]. Remarkably, this process may generate greater amounts of $\bullet O_2^-$, which subsequently interacts with surface-bound water to yield additional •OH radicals, as confirmed by scavenger experiments. Consequently, the electron-hole pair achieves efficient separation by preventing recombination of the charge carriers [8,48]. Degradation is expected to proceed via additional hydroxylation and oxidation of phenolic compounds, owing to the •OH radical's preference for electron-rich aromatic structures. Previous studies reported that this pathway entails benzene ring hydroxylation, yielding 3-hydroxyacetaminophen, 4-aminophenol, hydroquinone, 1,4-benzoquinone, and acetamide [8,24,51,52]. However, ongoing oxidation of these intermediates could cause the aromatic ring to break apart, eventually forming acids, carbon dioxide, and water molecules. All in all, the total elimination of PCM could occurs via direct oxidation by h_{vb}^+, •OH and $\bullet O_2^-$ radicals, as depicted in Eqs. (19)(20). Fig. 9(b) shows the mechanism of PCM degradation by MCC-Ag_2CO_3 composite photocatalyst.

$$MCC - Ag_2CO_3 \xrightarrow{h\nu} e_{cb}^- + h_{vb}^+, \quad (13)$$

$$h_{vb}^+ (Ag_2CO_3) + H_2O \rightarrow \bullet OH + H^+, \quad (14)$$

$$e_{cb}^- (MCC) + O_2 \rightarrow \bullet O_2^-, \quad (15)$$

$$\bullet O_2^- + 2H^+ + e_{cb}^- \rightarrow H_2O_2, \quad (16)$$

$$H_2O_2 + 2e_{cb}^- \rightarrow \bullet OH + OH^-, \quad (17)$$

$$OH^- + h_{vb}^+ \rightarrow \bullet OH, \quad (18)$$

$$h_{vb}^+ + PCM \rightarrow intermediates + CO_2 + H_2O, \quad (19)$$

$$\bullet O_2^- + \bullet OH + PCM \rightarrow intermediates + CO_2 + H_2O. \quad (20)$$

3.6. Photostability of MCC-Ag_2CO_3 photocatalyst

In the context of practical water treatment applications, photocatalyst stability represents a crucial factor. To evaluate the photostability and reusability of the MCC-Ag_2CO_3 composite photocatalyst for PCM degradation, a 10 mg/L PCM solution was irradiated under UVC light for 180 min at its native pH. After each cycle, the photocatalyst was recovered through filtration and rinsed with distilled water before reused it with a fresh batch of working solution. The filtered photocatalyst was reutilized for the next cycles without any chemical pre-treatments. As demonstrated in Fig. 10, the composite photocatalyst exhibited sustained high photodegradation efficiency of >50% over five consecutive cycles proving it strong stability. However, a noticeable decline in degradation efficiency was observed during the fifth cycle, which could be attributed to Ag_2CO_3's photo-corrosion after a long utilization under the UVC irradiation. Moreover, the decline in photodegradation performance may also resulted from the loss of photocatalysts during the recovery and decantation processes. Nevertheless, the composite photocatalyst's ability to maintain both high photodegradation performance and operational stability over multiple cycles demonstrated its promising potential for practical water treatment applications.

3.7. Structural stability of MCC-Ag_2CO_3 after photostability test

The structural stability of the MCC-Ag_2CO_3 composite after repeated photodegradation experiments was evaluated using FTIR spectroscopy. Fig. 11 shows the comparison of FTIR spectra and functionalities of the composite before and after the photostability test were carried out. The spectra of the MCC-Ag_2CO_3 composite photocatalyst exhibits characteristic peaks closely resembling those of pure Ag_2CO_3, with only slight shifts in wavenumber due to the small amount of MCC incorporated. The presence of CO_3^{2-} group is confirmed by peaks observed at 1387, 1317, 1071, 801, and 721 cm^{-1} [5,26,28]. These observations indicate that MCC incorporation does not significantly alter the Ag_2CO_3 structure, and the composite retains the functional groups responsible for photocatalytic activity. Furthermore, after the photostability test, the spectra show that all major peaks are preserved, confirming the structural sta-

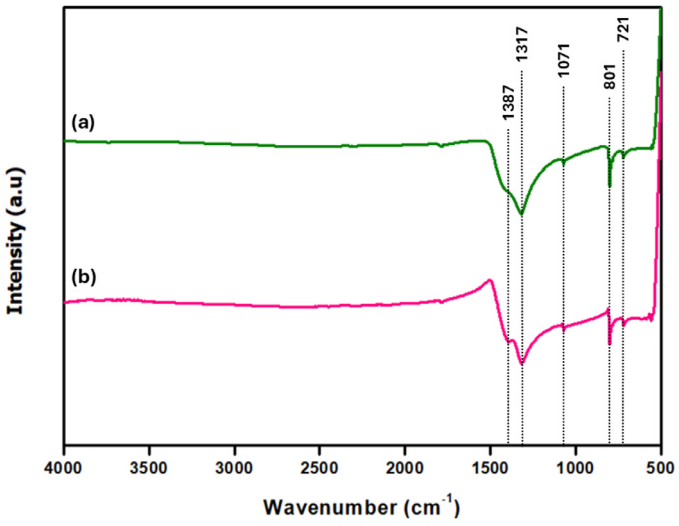

Fig. 11. FTIR spectra of MCC-Ag_2CO_3 composite photocatalyst for (a) before, and (b) after photostability test.

bility of the composite under long exposure of UVC irradiation. Notably, the peak around 1387 cm^{-1} exhibits a slight increase in intensity, which may be attributed to minor interactions between MCC and Ag_2CO_3 during photodegradation [5,8]. Overall, these results demonstrate that the MCC-Ag_2CO_3 composite retains its chemical structure and functional groups, supporting its durable and recyclable performance in photocatalytic applications.

4. Conclusion

This work successfully demonstrated the isolation of MCC from *Gigantochloa scortechinii* bamboo fibres and it's as an electron mediator for Ag_2CO_3, greatly enhanced its physicochemical properties and photocatalytic degradation performance. Characterization investigations indicated that pure MCC had a stick-like structures with a rough surface (diameter: 5.18 to 11.11 μm), while pure Ag_2CO_3 was observed to be rod-like microstructures and MCC-Ag_2CO_3 seems to consist of both morphologies. The integration of MCC increased the composite's crystallinity, reduced the band gap down to 2.6 eV, and PL quenching confirming efficient e_{cb}^-/h_{vb}^+ separation. The XPS spectrum identified two primary peaks at 368.4 and 374.4 eV which belongs to the Ag $3d_{5/2}$ and Ag $3d_{3/2}$ with standard chemical state difference of 6 eV. Through DFT analysis, the MCC-Ag_2CO_3 composite photocatalyst undergoes high orbital hybridization that remarkably reduces the band gap and improves charge carriers' delocalization. As confirmed by the absorption spectra, where the composite photocatalyst shows a clear red shift from ~1.34 to ~1.00 eV alongside higher absorption intensity across the spectrum. The band diagram further reveals the MCC facilitates interfacial charge transfer and suppresses recombination by providing conductive pathways and mid-gap states. In photocatalytic degradation tests, MCC-Ag_2CO_3 composite photocatalyst outperformed pure Ag_2CO_3 for PCM up to 82% efficiency under low-intensity of UVC irradiation. The photodegradation process followed the pseudo first-order model, with a maximum rate constant of 9.4×10^{-3} min^{-1} at the original pH of 6.8. In the scavenging study, h_{vb}^+ was observed as the main reactive species, followed by $\bullet O_2^-$ and •OH. The MCC-Ag_2CO_3 composite's stability was tested over five cycles, and it demonstrated outstanding reusability with minimum mass loss, with the percentage photodegradation retained of more than 50%. The MCC-Ag_2CO_3 composite photocatalyst maintained its structural integrity and photocatalytic activity after continuous uses, demonstrating the photocatalyst's resilience and potential long-term application for practical wastewater treatment.

Declaration of Competing Interest

The authors declare that they have no known competing financial interests or personal relationships that could have appeared to influence the work reported in this paper.

CRediT authorship contribution statement

Nurul Syarima Nadia Sazman: Writing – original draft, Investigation, Formal analysis, Data curation. **Nor Husnina Nor Shamsi:** Investigation, Formal analysis. **Nur Hafiz Hussin:** Validation, Software, Investigation, Data curation. **Mohamad Syafie Mahmood:** Validation, Conceptualization. **Fariza Aina Abd Manan:** Visualization, Methodology, Conceptualization. **Hamizah Mokhtar:** Resources, Project administration. **Hartini Ahmad Rafaie:** Supervision, Methodology. **Shaari Daud:** Supervision, Resources, Methodology. **Zul Adlan Mohd Hir:** Writing – review & editing, Supervision, Project administration, Methodology, Funding acquisition, Conceptualization.

Acknowledgements

This research was funded by Ministry of Higher Education, Malaysia under the Fundamental Research Grant Scheme (Project Number: FRGS/1/2024/STG05/UITM/02/12), as well as the services and facilities provided by UiTM Pahang Branch to carry out the laboratory work. The authors further expressed their sincere appreciation to the Ionic Materials and Devices Laboratory, Institute of Science, Universiti Teknologi MARA (UiTM) Shah Alam, for providing access to the computational facilities and CASTEP module used in the Density functional theory (DFT) calculations.

References

[1] W. Alamaw, A.M. Taddesse, A. Adgo, Z. Bezu, E. Teju, Synthesis and characterization of zeolite-supported CdS/TiO_2/Ag_2CO_3 ternary composite for photodegradation of methyl orange, Results Chem. 14 (2025) 102063, doi:10.1016/j.rechem.2025.102063.

[2] S. Behravesh, N. Mirghaffari, A.A. Alemrajabi, F. Davar, M. Soleimani, Photocatalytic degradation of acetaminophen and codeine medicines using a novel zeolite-supported TiO_2 and ZnO under UV and sunlight irradiation, Environ. Sci. Pollut. Res. 27 (2020) 26929–26942, doi:10.1007/s11356-020-09038-y.

[3] A. Irshad, M.H.H. Mahmoudb, R.Umer Usman, M. Naeem, I.H. El Azab, Z.M. El-bahy, Investigation of photocatalytic degradation of diclofenac sodium and acetaminophen by Zn-Ag co-doped barium hexaferrite@CNTs composite, Desalin. Water Treat. J. 319 (2024) 100415, doi:10.1016/j.dwt.2024.100415.

[4] F.H. Abdullah, N.H.H.A. Bakar, M.A. Bakar, Current advancements on the fabrication, modification, and industrial application of zinc oxide as photocatalyst in the removal of organic and inorganic contaminants in aquatic systems, J. Hazard. Mater. 424 (2022) 127416, doi:10.1016/j.jhazmat.2021.127416.

[5] Z. Huang, X. Qiu, D. Chen, X. Wu, S. Zhang, P. Zhu, Construction of Ag_2CO_3/$ZnFe_2O_4$/bentonite Z-type heterojunction photocatalyst and efficient degradation of norfloxacin, Opt. Mater. 143 (2023) 114153, doi:10.1016/j.optmat.2023.114153.

[6] K. Abhimanyu, H. Singh, S. Sable, V.K. Sonu, P. Singh, A. Kaushik, P. Thakur, V. Chaudhary, Exploring complex silver sulfide nano-systems as efficient photocatalysts for wastewater remediation and clean energy production: Toward sustainable and circular economy, Mater. Today 90 (2025) 681–705, doi:10.1016/j.mattod.2025.09.004.

[7] N. Thakur, A. Panwar, V. Soni, P. Raizada, P. Singh, A. Aslam, P. Khan, V. Nguyen, C.C. Nguyen, S.J. Yang, Q. Van Le, H. Kim, S. Sonu, Next-generation wastewater treatment with emerging 2D MOF-derived photocatalysts, ACS Omega 10 (2025) 58029–58056, doi:10.1021/acsomega.5c08223.

[8] N.S.N. Sazman, Z.A.M. Hir, S. Daud, H.A. Rafaie, Charge transport properties and photostability of microcrystalline cellulose derived from Gigantochloa scortechinii-supported ZnO for enhanced acetaminophen degradation, Ind. Crops Prod. 222 (2024) 119558, doi:10.1016/j.indcrop.2024.119558.

[9] S. Qiu, H. Hao, Z. Liu, Y. Li, X. Liu, T. Liu, Anchoring movable Ag_2CO_3 quantum dots on g-C_3N_4 with rich oxygen vacancies for enhanced simulated-sunlight CO_2 reduction in water medium, Sep. Purif. Technol. 330 (2024) 125330, doi:10.1016/j.seppur.2023.125330.

[10] H.A. Rafaie, N.I.T. Ramli, Z. Khusaimi, M.A.M. Sarjidan, P. Dulyaseree, Z.M.H. Adlan, Ag_2CO_3-based photocatalyst with enhanced photocatalytic activity for endocrine-disrupting chemicals degradation: A review, Catalysts 13 (2023) 540, doi:10.3390/catal13030540.

[11] P. Raizada, A. Sudhaik, P. Singh, P. Shandilya, P. Thakur, H. Jung, Visible light assisted photodegradation of 2,4-dinitrophenol using Ag_2CO_3 loaded phosphorus

and sulphur co-doped graphitic carbon nitride nanosheets in simulated wastewater, Arab. J. Chem. 13 (2020) 3196–3209, doi:10.1016/j.arabjc.2018.10.004.
[12] H. Xu, Y. Zhang, Y. Wang, L. Zhang, Z. Zhang, L. Zhong, Z. He, Y. Zheng, Y. Shen, Heterojunction material $BiYO_3$/g-C_3N_4 modified with cellulose nanofibers for photocatalytic degradation of tetracycline, Carbohydr. Polym. 312 (2023) 120829, doi:10.1016/j.carbpol.2023.120829.
[13] J. Nie, C. Li, Z. Jin, W. Hu, J. Wang, T. Huang, Y. Wang, Fabrication of MCC/Cu_2O/GO composite foam with high photocatalytic degradation ability toward methylene blue, Carbohydr. Polym. 223 (2019) 115101, doi:10.1016/j.carbpol.2019.115101.
[14] N.S.N. Sazman, H.A. Rafaie, S. Daud, N.A.M. Shohaimi, M.A.A.A. Bakar, Z.A.M. Hir, Extraction and physicochemical characterization of microcrystalline cellulose from Gigantochloa scortechinii, Malaysian J. Chem. 25 (2023) 323–330, doi:10.55373/mjchem.v25i3.323.
[15] C. Hua, X. Liu, S. Ren, C. Zhang, W. Liu, Preparation of visible light-responsive photocatalytic paper containing $BiVO_4$@diatomite/MCC/PVBCFs for degradation of organic pollutants, Ecotoxicol. Environ. Saf. 202 (2020) 110897, doi:10.1016/j.ecoenv.2020.110897.
[16] N. Amaly, A.Y. El-moghazy, N. Nitin, G. Sun, P.K. Pandey, Synergistic adsorption-photocatalytic degradation of tetracycline by microcrystalline cellulose composite aerogel dopped with montmorillonite hosted methylene blue, Chem. Eng. J. 430 (2022) 133077, doi:10.1016/j.cej.2021.133077.
[17] X. Li, L. Zhang, Z. Wang, S. Wu, J. Ma, Cellulose controlled zinc oxide nanoparticles with adjustable morphology and their photocatalytic performances, Carbohydr. Polym. 259 (2021) 117752, doi:10.1016/j.carbpol.2021.117752.
[18] N.S.N. Sazman, N.I. Izhar, N.R.M. Azaludin, S. Daud, H.A. Rafaie, Z.A.M. Hir, Valorization of wood waste as biosorbent for the removal of organic and inorganic contaminants in water, in: S.N. Sarmin, M. Jawaid, R. Elias (Eds.), Wood Waste Management and Products, Sustainable Materials and Technology, Springer, Singapore, 2023, pp. 59–78, doi:10.1007/978-981-99-1905-5_6.
[19] H. Xi, Q. Kang, D. Liu, H. Wang, W. Lu, Y. Zhao, X. Xu, Z. Yang, Z. Lei, Synthesis of C/BiOCl/Bi_2S_3 heterojunction photocatalyst induced by sodium carboxymethyl cellulose and its photocatalytic performance, Colloids Surf. A 724 (2025) 137498, doi:10.1016/j.colsurfa.2025.137498.
[20] C.C. Boungou, G.D. Ngantso, B.R. Malonda-Boungou, A.T. Raji, P.S. Moussounda, DFT calculations with and without spin polarization of the adsorption and decomposition of NCO and OCN on the Ag(110) surface, Comput. Condens. Matter 41 (2024) e00975, doi:10.1016/j.cocom.2024.e00975.
[21] M.F.M. Taib, M.K. Yaakob, O.H. Hassan, M.Z.A. Yahya, Structural, electronic, and lattice dynamics of $PbTiO_3$, $SnTiO_3$, and $SnZrO_3$: A comparative first-principles study, Integr. Ferroelectr. 142 (2013) 119–127, doi:10.1080/10584587.2013.780528.
[22] W. Kohn, L.J. Sham, Self-consistent equations including exchange and correlation effects, Phys. Rev. 140 (1965) A1133–A1138, doi:10.1103/PhysRev.140.A1133.
[23] H. Mukhair, A.H. Abdullah, Z.A.M. Hir, N.S. Osman, Z. Zainal, L.H. Ngee, In-depth investigation on the photostability and charge separation mechanism of Ag_3PO_4/g-C_3N_4 photocatalyst towards very low visible light intensity, J. Mol. Liq. 376 (2023) 121494, doi:10.1016/j.molliq.2023.121494.
[24] M. Chijioke-Okere, A.H. Abdullah, Z.A.M. Hir, J.I. Alinnor, E.E. Oguzie, Efficient photodegradation of paracetamol by integrated PES-ZnO photocatalyst sheets, Inorg. Chem. Commun. 148 (2023) 110377, doi:10.1016/j.inoche.2022.110377.
[25] M. Zhou, X. Tian, H. Yu, Z. Wang, C. Ren, L. Zhou, Y. Lin, L. Dou, WO_3/Ag_2CO_3 mixed photocatalyst with enhanced photocatalytic activity for organic dye degradation, ACS Omega 6 (2021) 26439–26453, doi:10.1021/acsomega.1c03694.
[26] A.S. Ganie, S. Hussain, A.A. Bhat, A. Farooq, R.K. Manavalan, A.M. Fouda, G. Qiao, G. Liu, Preparation of bifunctional Ag_2CO_3 decorated $BiVO_4$ nanospheres for high-performance electrochemical energy storage and photocatalytic activity, Surf. Interfaces 57 (2025) 105756, doi:10.1016/j.surfin.2025.105756.
[27] H. Sun, P. Qin, Z. Wu, C. Liao, J. Guo, S. Luo, Y. Chai, Visible light-driven photocatalytic degradation of organic pollutants by a novel Ag_3VO_4/Ag_2CO_3 p-n heterojunction photocatalyst: Mechanistic insight and degradation pathways, J. Alloys Compd. 834 (2020) 155211, doi:10.1016/j.jallcom.2020.155521.
[28] Y. Li, Z. Chen, Y. Liu, Y. Xu, J. Ma, Y. Guo, Ternary photocatalyst Bi_5O_7I/$Bi_2O_2CO_3$/Ag_2CO_3 with double Z-scheme heterojunction for the degradation of levofloxacin under visible light: Practical application and DFT calculation, J. Alloys Compd. 1010 (2025) 177294, doi:10.1016/j.jallcom.2024.177294.
[29] L.V. Bora, R.K. Mewada, Photocatalytic treatment of dye wastewater and parametric study using a novel Z-scheme Ag_2CO_3/SiC photocatalyst under natural sunlight, J. Environ. Chem. Eng. 5 (2017) 5556–5565, doi:10.1016/j.jece.2017.10.037.
[30] X. Shen, S. Yang, Y. Yang, Z. Yu, S. Liu, S. Shan, X. Wang, Q. Xue, Efficient degradation of norfloxacin by BiOBr/Ag_2CO_3 Z-type semiconductor heterojunction: Mechanistic insights and degradation pathways, Colloids Surf. A 709 (2025) 136135, doi:10.1016/j.colsurfa.2025.136135.
[31] L. Wang, J. Wang, M. Tang, C. Wang, D. Gao, Y. Zhou, Developing a Z-scheme Ag_2CO_3/ZIF-8 heterojunction for the surface decoration of cotton fabric toward repeatable photocatalytic dye degradation, Appl. Surf. Sci. 610 (2023) 155605, doi:10.1016/j.apsusc.2022.155605.
[32] A. Rebekah, R.P. V, K.S. Lee, Exploring visible light driven WO_3/Ag_2CO_3 embedded with reduced graphene oxide for enhancement of photocatalytic application, Colloids Surf. A 708 (2025) 136028, doi:10.1016/j.colsurfa.2024.136028.
[33] C. Teng, Y. Chen, Z. Tang, W. Yuan, L. Zhang, Y. Guo, F. Li, Q. Huang, Synthesis of Ag_2CO_3/TiO_2/SiC with pH stability and chloride ion boosted for efficient photodegrading tetracycline under visible light, Chem. Eng. J. 488 (2024) 150983, doi:10.1016/j.cej.2024.150983.
[34] R. Cao, H. Yang, X. Deng, S. Zhang, X. Xu, In-situ synthesis of amorphous silver silicate/carbonate composites for selective visible-light photocatalytic decomposition, Sci. Rep. 3 (2017) 15001, doi:10.1038/s41598-017-15405-6.
[35] N. Wang, L. Shi, L. Yao, C. Lu, Y. Shia, J. Sun, Highly improved visible-light-induced photocatalytic performance over BiOI/Ag_2CO_3 heterojunctions, RSC Adv. 8 (2018) 537–546, doi:10.1039/c7ra10423e.
[36] A. Moradbak, P.M. Tahir, A.Z. Mohamed, M.M. Abdi, R.L. Razalli, R. Halis, Isolation of cellulose nanocrystals from Gigantochloa scortechinii ASAM pulp, Eur. J. Wood Wood Prod. 76 (2018) 1021–1027, doi:10.1007/s00107-017-1244-1.
[37] T. Suparanon, S. Kaewchuy, N. Phusunti, V. Suchaiya, W. Phetwarotai, Synergistic effect of microcrystalline cellulose from oil palm empty fruit bunch waste and tricresyl phosphate on the properties of polylactide composites, Int. J. Biol. Macromol. 220 (2022) 1480–1492, doi:10.1016/j.ijbiomac.2022.09.140.
[38] S. Ventura-Cruz, N. Flores-Alamo, A. Tecante, Preparation of microcrystalline cellulose from residual Rose stems (Rosa spp.) by successive delignification with alkaline hydrogen peroxide, Int. J. Biol. Macromol. 155 (2020) 324–329, doi:10.1016/j.ijbiomac.2020.03.222.
[39] M.K. Hassan, M. Karim, D. Howlader, M.M. Alam, A. Kukmer, Comparative studies of Ag_3PO_4, Ag_2CO_3, and Ag_3VO_4 as photocatalyst for wastewater treatment: A first-principles calculation, Heliyon 9 (2023) e22757, doi:10.1016/j.heliyon.2023.e22757.
[40] A. Sudhaik, P. Raizada, T. Ahamad, S.M. Alshehri, V. Nguyen, Q. Van Le, S. Thakur, V. Kumar, R. Selvasembian, P. Singh, Recent advances in cellulose supported photocatalysis for pollutant mitigation: A review, Int. J. Biol. Macromol. 226 (2023) 1284–1308, doi:10.1016/j.ijbiomac.2022.11.241.
[41] H. Dong, G. Chen, J. Sun, C. Li, Y. Yu, D. Chen, A novel high-efficiency visible-light sensitive Ag_2CO_3 photocatalyst with universal photodegradation performances: Simple synthesis, reaction mechanism and first-principles study, Appl. Catal. B Environ. 134 (2013) 46–54, doi:10.1016/j.apcatb.2012.12.041.
[42] S. Li, X. Li, Y. Liu, P. Zhang, J. Zhang, B. Zhang, Interfacial engineering of a plasmonic Ag/Ag_2CO_3/C_3N_5 S-scheme heterojunction for high-performance photocatalytic degradation of antibiotics, Chinese J. Catal. 72 (2025) 130–142, doi:10.1016/S1872-2067(25)64652-3.
[43] I. Rouibah, S. Hakimi, N. Khellaf, H. Ben Mansour, A.A. Assadi, Photoactivity performance of TiO_2/cellulose and ZnO/polystyrene; intensified effect of oxidants on degradation efficiency of acetaminophen, Phys. Chem. Res. 9 (2021) 413–426, doi:10.22036/pcr.2020.243655.1810.
[44] C. Shi, L. Zhang, H. Bian, Z. Shi, J. Ma, Z. Wang, Construction of Ag-ZnO/cellulose nanocomposites via tunable cellulose size for improving photocatalytic performance, J. Clean. Prod. 288 (2021) 125089, doi:10.1016/j.jclepro.2020.125089.
[45] M.F.H. Hashim, Z.A.M. Hir, S. Daud, H.A. Rafaie, H. Mokhtar, M.A. Mohamed, Microcrystalline cellulose from kapok fiber (Ceiba pentandra) as carbon interstitial dopant in ZnO: Physicochemical characteristics and photocatalytic activity, Environ. Qual. Manag. 35 (2025) e70199, doi:10.1002/tqem.70199.
[46] J. Li, R. Guan, J. Zhang, Z. Zhao, H. Zhai, D. Sun, Y. Qi, Preparation and photocatalytic performance of dumbbell Ag_2CO_3-ZnO heterojunctions, ACS Omega 5 (2020) 570–577, doi:10.1021/acsomega.9b03131.
[47] M.O. Chijioke-Okere, Z.A.M. Hir, C.E. Ogukwe, P.C. Njoku, A.H. Abdullah, E.E. Oguzie, TiO_2/polyethersulphone films for photocatalytic degradation of acetaminophen in aqueous solution, J. Mol. Liq. 338 (2021) 116692, doi:10.1016/j.molliq.2021.116692.
[48] S. Qiu, H. Hao, Z. Liu, Y. Li, X. Liu, T. Liu, Anchoring movable Ag_2CO_3 quantum dots on g-C_3N_4 with rich oxygen vacancies for enhanced simulated-sunlight CO_2 reduction in water medium, Sep. Purif. Technol. 330 (2024) 125330, doi:10.1016/j.seppur.2023.125330.
[49] N. Pan, S. Liu, Y. Han, D. Li, J. Chai, A comparison study of the performance of Ag_2CO_3 photocatalysts synthesized respectively in a surfactant-free microemulsion, water, and a water/propan-2-ol mixture, J. Mater. 8 (2022) 781–789, doi:10.1016/j.jmat.2022.02.006.
[50] M. Hasanpour, M. Hatami, Photocatalytic performance of aerogels for organic dyes removal from wastewaters: Review study, J. Mol. Liq. 309 (2020) 113094, doi:10.1016/j.molliq.2020.113094.
[51] E. Moctezuma, E. Leyva, C.A. Aguilar, R.A. Luna, C. Montalvo, Photocatalytic degradation of paracetamol: Intermediates and total reaction mechanism, J. Hazard. Mater. 243 (2012) 130–138, doi:10.1016/j.jhazmat.2012.10.010.
[52] V.H.T. Thi, B.K. Lee, Effective photocatalytic degradation of paracetamol using La-doped ZnO photocatalyst under visible light irradiation, Mater. Res. Bull. 96 (2017) 171–182, doi:10.1016/j.materresbull.2017.04.028.